



South Asia ammonia emission inversion through assimilating IASI observations

Ji Xia^{1,*}, Yi Zhou^{2,*}, Li Fang¹, Yingfei Qi³, Dehao Li¹, Hong Liao¹, and Jianbing Jin¹

¹Joint International Research Laboratory of Climate and Environment Change, Jiangsu Key Laboratory of Atmospheric Environment Monitoring and Pollution Control, Jiangsu Collaborative Innovation Center of Atmospheric Environment and Equipment Technology, School of Environmental Science and Engineering, Nanjing University of Information Science and Technology, Nanjing, Jiangsu, China

²School of Management Science and Engineering, Nanjing University of Information Science and Technology, Nanjing, Jiangsu, China

³College of Geography and Remote Sensing, Hohai University, Nanjing, Jiangsu, China

*These authors contributed equally to this work.

Correspondence: Jianbing Jin (jianbing.jin@nuist.edu.cn)

Abstract. Ammonia has attracted significant attention due to its pivotal role in the ecosystem and its contribution to the formation of secondary aerosols. Developing an accurate ammonia emission inventory is crucial for simulating atmospheric ammonia levels and quantifying its impacts. However, current inventories are typically constructed in the bottom-up approach and are associated with substantial uncertainties. To address this issue, assimilating observations from satellite instruments for top-down emission inversion has emerged as an effective strategy for optimizing emission inventories. Despite the severity of ammonia pollution in South Asia, research in this context remains very limited. This study aims to estimate ammonia emissions in this region by integrating the prior emission inventory from the Community Emissions Data System (CEDS) and the columned ammonia concentration retrievals from the Infrared Atmospheric Sounder Interferometer (IASI). We employ a newly-developed four-dimensional ensemble variational (4DEnVar)-based emission inversion system to conduct the calculations, resulting in monthly ammonia emissions for 2019 at a resolution of $0.5^\circ \times 0.625^\circ$. Our simulations, driven by the posterior emission inventory, demonstrate superior performance compared to those driven by the prior emission inventory. This is validated through comparisons against the IASI observations, the independent column concentration measurements from the advanced satellite instrument Cross-track Infrared Sounder (CrIS), and the ground concentration observations of ammonia and $PM_{2.5}$. Additionally, the spatial and temporal characteristics of ammonia emissions in South Asia based on the posterior are analyzed. Notably, emissions there exhibit a "double-peak" seasonal profile, with the maximum in July and the secondary peak in May. This differs from the "double-peak" trend suggested by the CEDS prior inventory, which identifies the maximum in May and a second peak in September.

1 Introduction

Ammonia (NH_3), an alkaline compound, has the capacity to react with acidic gases present in the atmosphere, thereby contributing to the formation of secondary aerosols, notably ammonium sulfate and ammonium nitrate (Jimenez et al., 2009).



The genesis of fine atmospheric particulate matter poses significant threats to human health (Mukherjee and Agrawal, 2017). Further, ammonia gas, along with its reaction products, plays a pivotal role in soil acidification and the eutrophication of water bodies through both dry and wet deposition (Krupa, 2003), and thereby affecting the balance of ecosystems (Asman et al., 1998) and climate change (Sanderson et al., 2006). With an enormous livestock population and extensive use of nitrogen fertilizers, South Asia has experienced the highest level of atmospheric NH_3 globally (Pawar et al., 2021b; Luo et al., 2022).

Over the past decade, scientists have predominantly employed the "bottom-up" approach to estimate ammonia emissions. When combined with chemical transport models, atmospheric ammonia dynamics can be simulated, and the environmental impacts can be quantified. Substantial efforts have been made to quantify the spatiotemporal distribution of ammonia sources and develop global/regional emission inventories, such as the global ammonia emission inventory (Bouwman et al., 1997), the anthropogenic emission inventory that includes ammonia estimates (e.g., Community Emissions Data System, CEDS) (Hoesly et al., 2018), as well as regional NH_3 inventories focusing on South Asia (Yan et al., 2003; Yamaji et al., 2004; Liu et al., 2022). However, these bottom-up estimates of NH_3 emissions are generally considered uncertain (Xu et al., 2019), especially compared to other pollutants mainly derived from fossil fuel combustion (e.g., NO_2). One challenge is that the intensity of agricultural NH_3 emissions (i.e., emission factors), whether from livestock or fertilizer, depends heavily on management and farming practices, but this information is often not readily available (Zhang et al., 2017). As a result, atmospheric chemistry transport models driven by these emission estimates inevitably struggle to reproduce atmospheric ammonia concentrations. Consequently, these discrepancies hinder our comprehensive understanding of the environmental implications of ammonia emissions.

The rapid advancement of satellite remote sensing technology has resulted in an expanding array of valuable ammonia products, such as those from the first satellite ammonia observations using the Tropospheric Emission Spectrometer (TES) (Beer et al., 2008), as well as higher-resolution retrievals from the Infrared Atmospheric Sounding Interferometer (IASI) (Pawar et al., 2021b) and the Cross-track Infrared Sounder (CrIS) (Beale et al., 2022; Kharol et al., 2022). While these remote sensing measurements play a pivotal role in characterizing atmospheric ammonia loading, limitations still remain. These primarily arise from the fact that satellite observations can only measure column-integrated ammonia concentrations, which do not directly reflect emission intensity or the three-dimensional concentration field. In addition to these satellite-based data, very limited ground-based observations are publicly available over South Asia, and those that do exist are constrained by their inadequate representation of atmospheric ammonia features (Pawar et al., 2021b).

In the field of atmospheric pollutant modeling, an alternative method for calculating emission flux is the "top-down" approach, which is achieved through data assimilation. Over the past decade, emission inversion has gained widespread attention globally and has been applied in various contexts, including the estimation of Volatile Organic Compounds (VOCs) (Bauwens et al., 2016; Choi et al., 2022), sulfur dioxide (SO_2) (Qu et al., 2019; Li et al., 2021), methane (CH_4) (Wecht et al., 2014; Fujita et al., 2020), and atmospheric ammonia emissions. For example, Kong et al. (2019) calculated the 2016 ammonia emission inventory in China by assimilating ground-based NH_3 concentration observations from several dozen ground stations. Similarly, Chen et al. (2021) optimized the prior NH_3 emission estimates from the United States' 2011 National Emissions Inventory (2011 NEI) by assimilating ammonia column concentrations from IASI instruments across the United States. Recently, we



developed a four-dimensional variational assimilation-based ammonia emission inversion system, which has been successfully tested in ammonia emission inversion by assimilating IASI products over China.

However, there is a paucity of studies focusing on assimilation-based ammonia emission inversion specific to South Asia, which has some of the highest ammonia loading hotspots compared to other continents. In this study, we aim to explore the spatial and temporal features of ammonia emissions over South Asia. The ammonia emission inventory will be calculated using our newly developed emission inversion system (Jin et al., 2023), by assimilating ammonia retrievals from the IASI instruments onboard MetOp-A (operational from 2008 to 2018), MetOp-B (operational since 2012), and MetOp-C (operational since 2018) satellites. Instead of directly assimilating IASI measurements as previous studies have done, we incorporated the averaging kernel information from the latest version of the IASI product. This approach allowed us to update the column concentration observations before assimilation. By doing so, we ensure a fairer comparison between the simulated and observed columnar ammonia concentrations, a point that has been emphasized in several studies (Eskes and Boersma, 2003; von Clarmann and Glatthor, 2019), but never implemented in the IASI-based emission inversion. The posterior ammonia emissions will be validated by comparing them with high-quality ammonia observations from the advanced CrIS product, as well as ground-based measurements of ammonia and PM_{2.5}. This study not only provides a more accurate estimation of ammonia emission inventories and explores their characteristics over South Asia, but also serves as an example of effectively calculating other atmospheric pollution emissions in regions that have received less attention in the past.

The remaining sections of this paper are organized as follows: Section 2 describes the measurements assimilated in the ammonia emission inversion, as well as those used for independent validation. The assimilation methodology for the emission inversion, along with the choice of the prior emission inventory and the chemical transport model, is also outlined. Section 3 presents the validation results of the emission inversion and highlights the key features of ammonia emissions over South Asia.

2 Data and method

2.1 IASI satellite measurements

IASI (Infrared Atmospheric Sounding Interferometer) is a Fourier Transform Spectrometer that operates in the thermal infrared spectral range. It is onboard the Meteorological Operational (MetOp) A/B/C satellites, a series of European polar-orbiting meteorological satellites managed by the European Space Agency (ESA) and the European Organization for the Exploitation of Meteorological Satellites (EUMETSAT). The first MetOp-A satellite, equipped with IASI, was launched in 2008, followed by MetOp-B and MetOp-C in 2012 and 2018, respectively. The IASI instruments operate at an altitude of 817 km in a sun-synchronous orbit with an inclination of 98.7°. Each instrument conducts measurements over a ground swath width of 2200 km, with 30 fields of view (15 on each side of the nadir). Each field of view consists of four pixels, each with a nadir diameter of 12 km. This observational strategy enables each IASI instrument to make two passes over every point on Earth daily, around 09:30 and 21:30 local time (Bouillon et al., 2020).

The assimilated observations for estimating the ammonia emissions were the monthly IASI column concentration means over the 0.5°×0.625°GEOS-Chem grid cell. These values were derived from the latest ANNI-NH₃-v4R-ERA5 product. De-



spite improvements in NH_3 column retrievals from satellite observations, there remains substantial variability in measurement uncertainty, ranging from 5 % to over 1000 %. (Van Damme et al., 2014; Whitburn et al., 2016; Van Damme et al., 2017). Data selection was performed by excluding nighttime observations and irrational values (<0) during the calculation of the monthly mean.

5 Compared to the previous version, one highlight of the latest version 4 product is that it includes averaging kernel information. The benefit of using the averaging kernel is that it can consider the vertical distribution characteristics of satellite observations, helping to correct the satellite retrieval results and making them more representative of the true distribution of the target gas or variable in the atmosphere (Rodgers, 2000). The impact of averaging kernels (AVKs) are supposed to be considered in the data processing. The sensitivity of IASI NH_3 observations varies with altitude, and AVKs enable the adjustment of simulated or observed NH_3 concentrations to align with the vertical distribution detected by IASI. This adjustment is particularly important for data comparison and validation against the model simulations (Clarisse et al., 2023). The formula for calculating the column concentration, after accounting for the averaging kernels, in this paper follows:

$$\hat{X}^m = \frac{\hat{X}^a - B}{\sum_z A_z^a m_z} + B. \quad (1)$$

here, \hat{X}^m represents the IASI column concentration retrieved with model profile. \hat{X}^a denotes the initial IASI column concentration, with the background concentration B. The A_z^a values are AVK for each vertical layer, with the model profile m_z .

The uncertainties of the IASI measurements is also the essential part in the assimilation. When calculating the uncertainty of gridded monthly average ammonia measurements, both instrumental errors $\sigma^{\text{instrumental}}$ and representation error $\sigma^{\text{representation}}$ are considered. The gridded average uncertainty derived directly from IASI products was designated as instrumental error $\sigma^{\text{instrumental}}$, while the standard deviation of the observed samples for the gridded average characterized representation error $\sigma^{\text{representation}}$. The total uncertainty σ^{total} for weighting the potential spread of the assimilated IASI ammonia measurements is finally expressed as:

$$\sigma^{\text{total}} = \left\{ (\sigma^{\text{instrument}})^2 + (\sigma^{\text{representing}})^2 \right\}^{0.5} \quad (2)$$

Four snapshots of the assimilated monthly IASI ammonia column concentration observations and their uncertainty in January, April, July and November can be found in Fig. 2 (a)-(b). These four scenarios are selected to highlight the typical seasonal profile of the ammonia loading over South Asia.

2.2 Independent observations for validation

The Crosstrack Infrared Sounder (CrIS) ammonia column concentration and ground-based observations of ammonia and $\text{PM}_{2.5}$ from the Central Pollution Control Board (CPCB) of India were also collected to validate our assimilation results.

The CrIS instrument was launched in 2011 on the Suomi National Polar-Orbiting Partnership (SNPP) satellite and in 2017 on the NOAA-20 satellite. The retrieval products from SNPP began in 2011 and ended in May 2021, with a data gap from April to August 2019. The NH_3 retrieval products from NOAA-20 started in March 2019. Therefore, we used retrieval



products from both SNPP and NOAA-20 as independent observations for 2019. We utilized the Level 2 CrIS product from the CFPR 1.6.4 version. Specifically, only the CrIS observations during daytime, under cloud-free conditions, and with a quality flag ≥ 3 were selected. These original data were subsequently interpolated to achieve a spatial resolution of $0.5^\circ \times 0.625^\circ$, which is consistent with our ammonia simulation. Similarly, we also considered the impact of the averaging kernels (AVKs) and applied the AVKs to the satellite profile data. We converted the logarithmic averaging kernels into linearized averaging kernels based on the method proposed by Cao et al. (2022).

Ground observations of ammonia in South Asia are mainly provided by the Central Pollution Control Board (CPCB, <https://cpcb.nic.in/>), which is the official portal of Government of India. NH_3 is measured by the chemiluminescence method as NO_x following the oxidation of NH_3 to NO_x . In that approach, NH_3 is determined from the difference between NO_x concentration with and without inclusion of NH_3 oxidation (Pawar et al., 2021b). The ground level ammonia concentration data from CPCB was successfully collected. There were ammonia surface concentration observations from 33 stations available in 2019, and the distribution are shown in Fig. 1.

$\text{PM}_{2.5}$ observations from CPCB were also used in the assimilation validation. The $\text{PM}_{2.5}$ observations were selected before they were used, which follows (Spandana et al., 2021): First, select the hourly $\text{PM}_{2.5}$ data greater than PM_{10} , then filter out the hourly $\text{PM}_{2.5}$ data that falls outside the range of $\text{day}_{mean} - 3 \times \text{standard deviation}$ and $\text{day}_{mean} + 3 \times \text{standard deviation}$. Additionally, ensure that each day contains at least 20 hours of data. Finally, the data is processed into monthly averages for subsequent validation. The distribution of the ground stations where the $\text{PM}_{2.5}$ were used in this paper can be found in Fig. 1.

2.3 Emission inversion system

This study employs the four-dimensional ensemble variational (4DEnVar) data assimilation -based ammonia emission inversion system that was developed by Jin et al. (2023). The general idea of assimilation-based emission inversion is to find the most likely estimate, which in this case is the monthly ammonia emission field, given the prior ammonia emissions and the observations. The calculation is conducted through minimizing the cost function \mathcal{J} :

$$\mathcal{J}(\mathbf{f}) = \frac{1}{2}(\mathbf{f} - \mathbf{f}_b)^T \mathbf{B}^{-1}(\mathbf{f} - \mathbf{f}_b) + \frac{1}{2}\{\mathbf{y} - \mathbf{H}\mathcal{M}(\mathbf{f})\}^T \mathbf{O}^{-1}\{\mathbf{y} - \mathbf{H}\mathcal{M}(\mathbf{f})\} \quad (3)$$

here, \mathbf{f}_b denotes the prior monthly ammonia emission vector from CEDS as will be described in Section 2.3.2. \mathbf{B} represents the background error covariance matrix associated with the prior emission estimate. Here we assumed that the uncertainty in the ammonia emission can be compensated by a spatially varying tuning factor α . The α values are defined to be random variables with a mean of 1.0 and a standard deviation $\sigma = 0.2$. In addition, a correlation matrix \mathbf{C} is introduced for quantifying the spatial correlation between two α s in the grid i and j as:

$$\mathbf{C}(i, j) = e^{-(d_{i,j}/l)^2/2} \quad (4)$$

where $d_{i,j}$ represents the distance between two grid cells i and j . l here denotes the correlation length scale which controls the spatially variability freedom of the α s. An empirical parameter $l = 300$ km which is used in the ammonia emission inversion

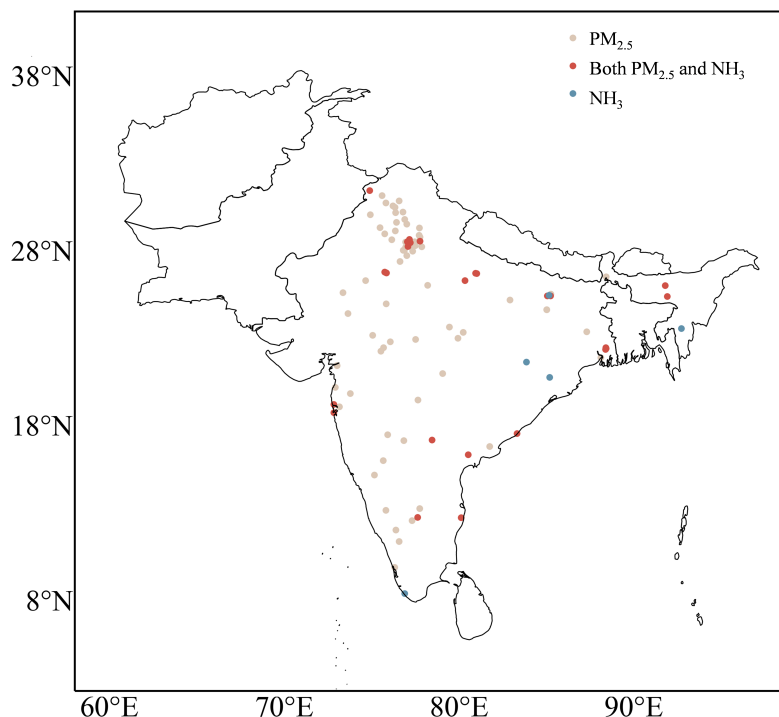


Figure 1. The GEOS-Chem model simulation domain, with dots indicating the locations of ground observation stations from the Central Pollution Control Board (CPCB), India. The three different colored dots represent stations with only $\text{PM}_{2.5}$ observations, stations with both $\text{PM}_{2.5}$ and NH_3 observations, and stations with only NH_3 observations, respectively.

in China (Jin et al., 2023) is also used in this study. With the spatial correlation matrix and the emission uncertainty, the background error covariance matrix could then be constructed as:

$$\mathbf{B}(i,j) = \sigma^2 \cdot \mathbf{f}(i) \cdot \mathbf{f}(j) \cdot \mathbf{C}(i,j) \quad (5)$$

\mathcal{M} here represents the GEOS-Chem model (as will be illustrated in Section 2.3.1) driven by the emission \mathbf{f} , \mathbf{H} here is the observational operator that transfer the simulated NH_3 3D concentration result into the observational space. \mathbf{y} represents the monthly IASI ammonia column concentration observations, while \mathbf{O} is the observation error covariance matrix. Here we assume IASI observations are independent on each other. \mathbf{O} therefore is a diagonal matrix filled with the square of the integrated uncertainty as illustrated in Section 2.1. Meanwhile, a minimum measurement error is used to prevent the posterior from being too close to low-value observations, thereby avoiding model divergence:

$$\mathbf{O}_{i,i} = \min \left(1.0 \times 10^{16} \text{ molec cm}^{-2}, \sigma^{\text{integrated}} \right)^2 \quad (6)$$

More information about how we minimizing the cost function Eq. 3 could be found in Jin et al. (2023).

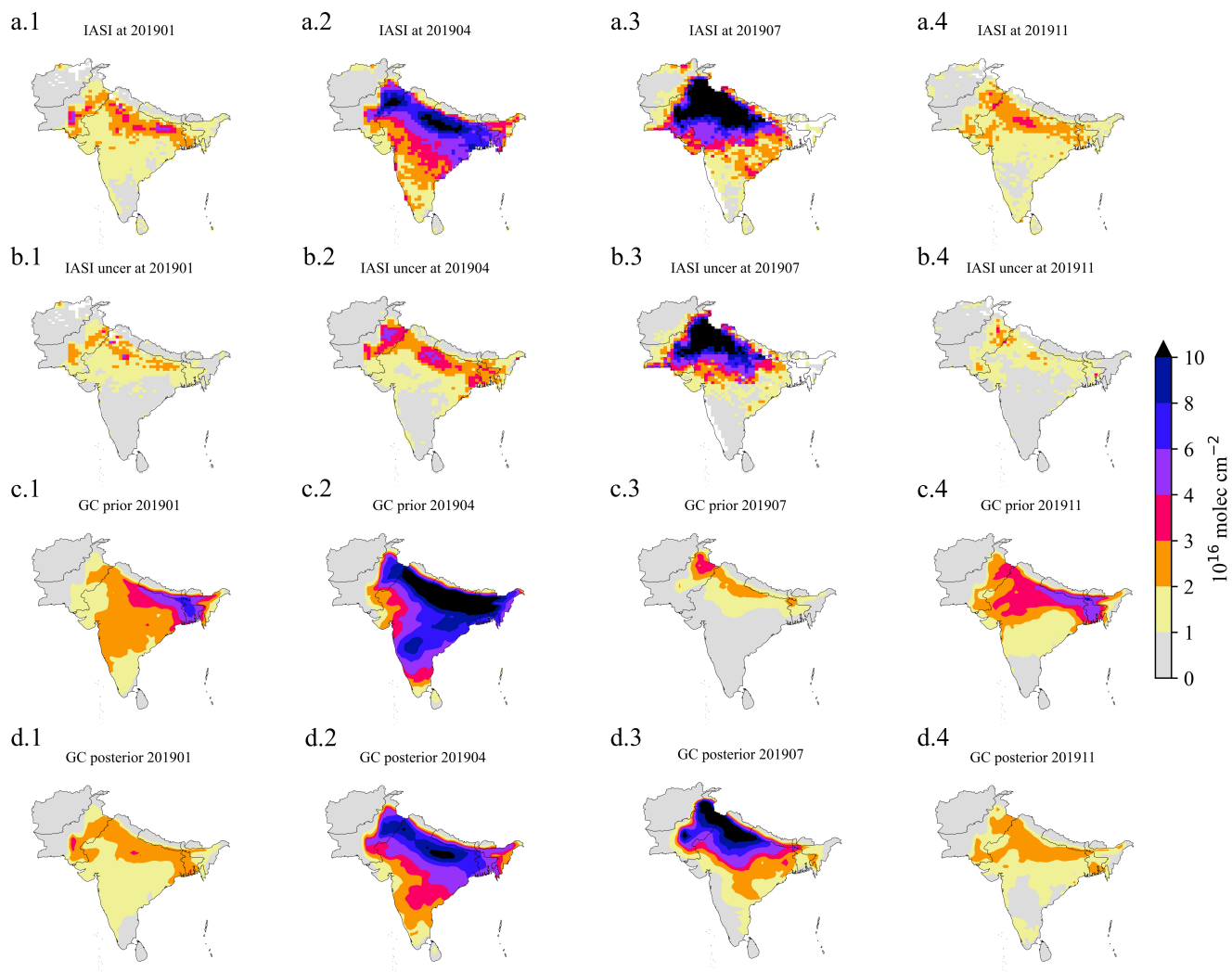


Figure 2. Spatial distribution of the total column ammonia concentration from IASI instruments (a) and its uncertainty (b), and from the GEOS-Chem simulation either using the prior (c) or using the posterior (d) NH_3 emission flux in 2019 January (a.1)–(d.1), April (a.2)–(d.2), July (a.3)–(d.3) and November (a.4)–(d.4).



2.3.1 GEOS-Chem model

GEOS-Chem, a three-dimensional (3-D) global tropospheric chemistry model, is driven by assimilated meteorological data obtained from the Goddard Earth Observing System (GEOS) at the NASA Data Assimilation Office (DAO) (Bey et al., 2001). GEOS-Chem incorporates a fully integrated chemistry system involving aerosol, ozone, NO_x , and hydrocarbons, as described by Park et al. (2004). The wet deposition scheme is explained by Liu et al. (2001) for water-soluble aerosols and by Amos et al. (2012) for gaseous components. Dry deposition is modeled using the resistance-in-series scheme proposed by Wesely and Lesht (1989), as applied by Wang and Jacob (1998). Size-specific aerosol dry deposition follows the approach outlined by Emerson et al. (2020).

A nested grid simulation within the GEOS-Chem model v13.4.1 is conducted to simulate the atmospheric environment over South Asia. The nested domain ($60^\circ\text{--}98^\circ\text{E}$, $4^\circ\text{--}40^\circ\text{N}$), shown in Fig. 1, has a horizontal resolution of 0.5° latitude by 0.625° longitude, accompanied by 47 vertical layers, with boundary conditions updated every 3 hours.

2.3.2 Prior ammonia emission inventory

The ammonia emissions inventory employed to drive GEOS-Chem originated from the Community Emissions Data System (CEDS, <https://doi.org/10.25584/PNNLDH/1854347>) inventory, which was widely used for modeling the South Asia atmospheric pollutants, e.g., VOCs (Chaliyakunnel et al., 2019), $\text{PM}_{2.5}$ pollution (Guttikunda and Nishadh, 2022; Xue et al., 2021). CEDS inventory includes various sources encompassing agricultural, energy production, industrial, residential and commercial activities, ships, solvent use, surface transportation, and waste processing (McDuffie et al., 2020), the bulk of ammonia emissions originate from agricultural practices. Specifically, these emissions stem predominantly from farmlands, including crops such as wheat, maize, and rice, as well as livestock waste, spanning cattle, chicken, goats, and pigs (Liu et al., 2022).

The CEDS emission estimates were coarse-grained into the model resolution $0.5^\circ \times 0.625^\circ$ before being utilized to drive the GEOS-Chem simulations. Examples of the CEDS emission over the South Asia are presented in Fig. 3, which plot the total ammonia emission fluxes for January, April, July, November of the year 2019.

3 Results and discussion

With the assimilation system described above, the monthly ammonia emission inversion for 2019 over South Asia is conducted. The posterior is evaluated in Section 3.1. The spatial distribution and the seasonal profile of the South Asia ammonia emission are analyzed and discussed based on the inversion results in Section 3.3, while Section 3.2 illustrated the long term varying trend.

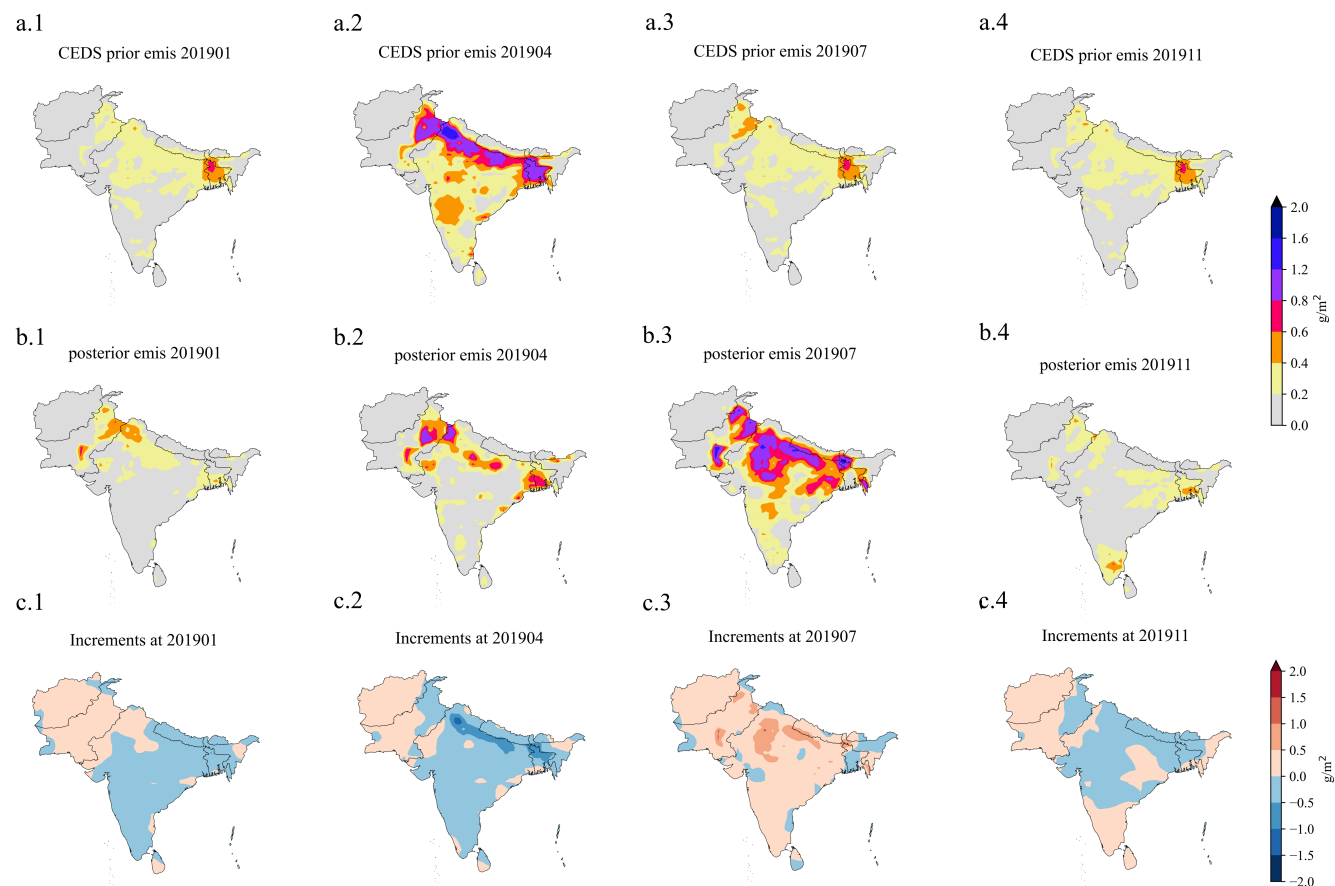


Figure 3. Spatial distribution of the prior (a), the posterior (b) and the posterior minus prior increments (c) monthly NH_3 emission in 2019 January (a.1)–(c.1), April (a.2)–(c.2), July (a.3)–(c.3) and November (a.4)–(c.4).

3.1 Validation

To evaluate our inversion results, we here compared the atmospheric ammonia simulation either driven by the posterior emission (refer to as the posterior simulation), or driven by the prior one against the observations, including the assimilated IASI column data, the independent CrIS retrieval and ground-based ammonia and $\text{PM}_{2.5}$ concentration measurements.

5 3.1.1 NH_3 total column concentration

The prior and posterior ammonia column concentration simulations for four months (January, April, July, and November) are presented in Fig. 2 (c)–(d), alongside the IASI measurements shown in panel (a). These months were selected as typical examples representing four different seasons. The column concentration distributions for the rest months from the model and satellite observations could be found in Figs. S1 and S2, respectively. While the prior simulation generally captured the



distribution of ammonia, with hot spots in North India, Pakistan, and Bengal—consistent with the IASI retrievals—it failed to capture the correct seasonal profile. According to the IASI measurements, ammonia concentrations peak in July, a pattern clearly visible in the monthly variation of the IASI-observed ammonia column concentrations from 2015 to 2023 as will be discussed in Section 3.2. However, the prior model incorrectly indicated that the highest ammonia loading occurred in the Spring and Autumn seasons. As a result, ammonia loading was severely overestimated in Winter and Spring (particularly in May) but significantly underestimated in Summer. The difference between the model and IASI observations for the entire year of 2019 is shown in Fig. 4 (a). The overestimation by the prior model is particularly evident in Spring (especially May), while the underestimation is most prominent in Summer (especially July). These discrepancies contributed to a relatively high model error, with the correlation coefficient (R) as low as 0.33 and the root mean square error (RMSE) as high as 4.64×10^{16} molec cm^{-2} . In contrast, the posterior emission-driven GEOS-Chem simulations showed good consistency with the IASI retrievals, capturing both the spatial and temporal variations, as shown in panel (d) of Fig. 2. This resulted in significantly improved performance, with R increasing to 0.76 and RMSE reducing to 2.48×10^{16} molec cm^{-2} , as shown in panel (b) of Fig. 4.

Note that there are still some discrepancies in the posterior simulation vs IASI column measurements. In particular, as shown in panel a.3 vs. d.3 of Fig. 2, the posterior simulation did not fully reproduce the extremely high ammonia loading observed by IASI in July (with column-integrated concentrations exceeding 10×10^{16} molec cm^{-2}). This discrepancy is also evident in the scatter plot of the posterior column simulation against the IASI measurements in panel (b) of Fig. 4. This occurs because the goal of the assimilation is to achieve the best fit between the posterior, the observations, and the prior emissions, rather than just fitting the observations alone. The extremely high ammonia concentrations are less likely given the relatively low prior ammonia emissions and the background error covariance matrix described in Section 2.3. Additionally, the 4DVar assimilation algorithm inherently accounts for potential model variations through ensemble simulations. However, the response of GEOS-Chem ammonia simulations to emission variations is nonlinear, making it difficult to accurately resolve these discrepancies through the 4DVar data assimilation algorithm without implementing outer-loop optimization strategies. In addition, we further evaluated our posterior simulations using the other advanced satellite ammonia product from the CrIS instruments. The scatter plots of the CrIS monthly ammonia column concentrations vs. the prior/posterior simulations in 2019 are presented in panels (a) and (b) of Fig. 5. Steady improvements were observed in the comparison against the independent CrIS retrievals, with the correlation coefficient (R) increasing from 0.42 to 0.71, and the root mean square error (RMSE) decreasing from 3.96 to 2.06×10^{16} molec cm^{-2} . The spatial distribution of the ammonia column concentrations observed by CrIS, as shown in Fig. 6, demonstrate good consistency with both the IASI observations and the posterior simulation results presented in Fig. 2. These evaluations give us confidence that our emission inversion has successfully calculated the most likely posterior, given both the prior and the IASI measurements.

3.1.2 NH_3 and $\text{PM}_{2.5}$ ground concentration validation

The few surface ammonia concentration observations from ground stations, shown in Fig. 1, were also utilized to evaluate our ammonia emission inversion results. Fig. 7 presents the scatter plot of monthly surface ammonia concentrations against the prior/posterior simulations. Our posterior results are in better agreement with these independent surface ammonia concentration

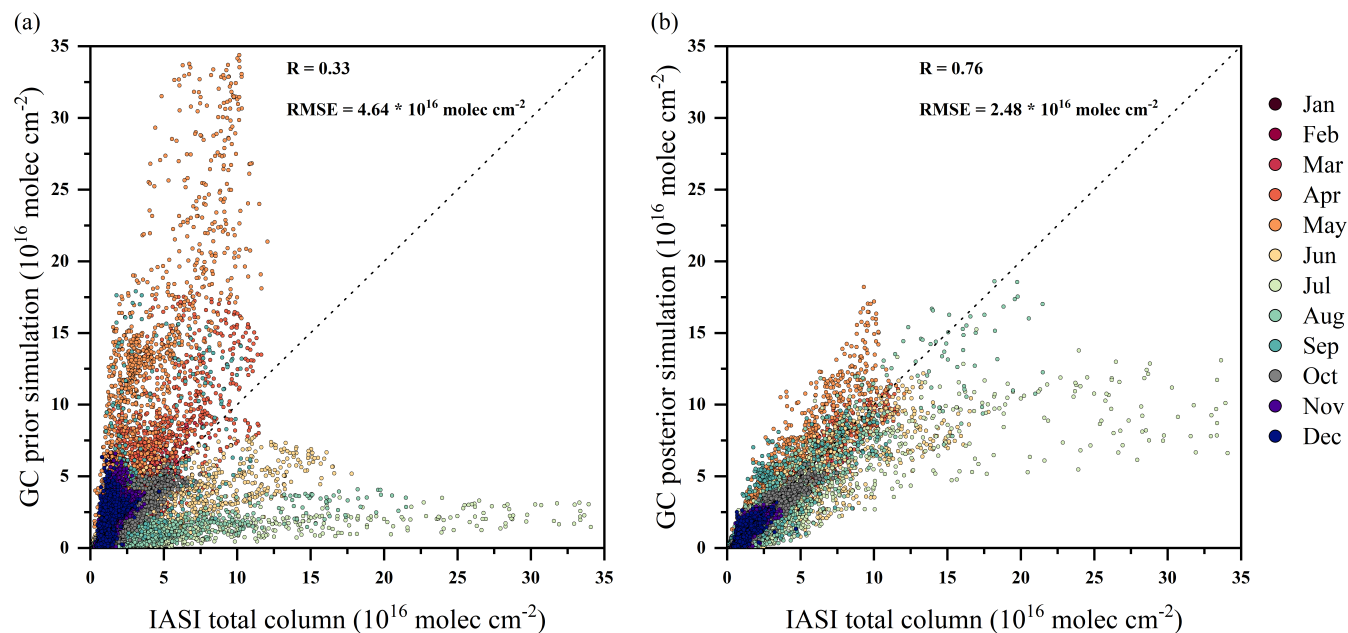


Figure 4. Scatter plot of the IASI-observed against the NH_3 simulation over South Asia either using the prior (a) or using the posterior (b) NH_3 emission inventory from January to December.

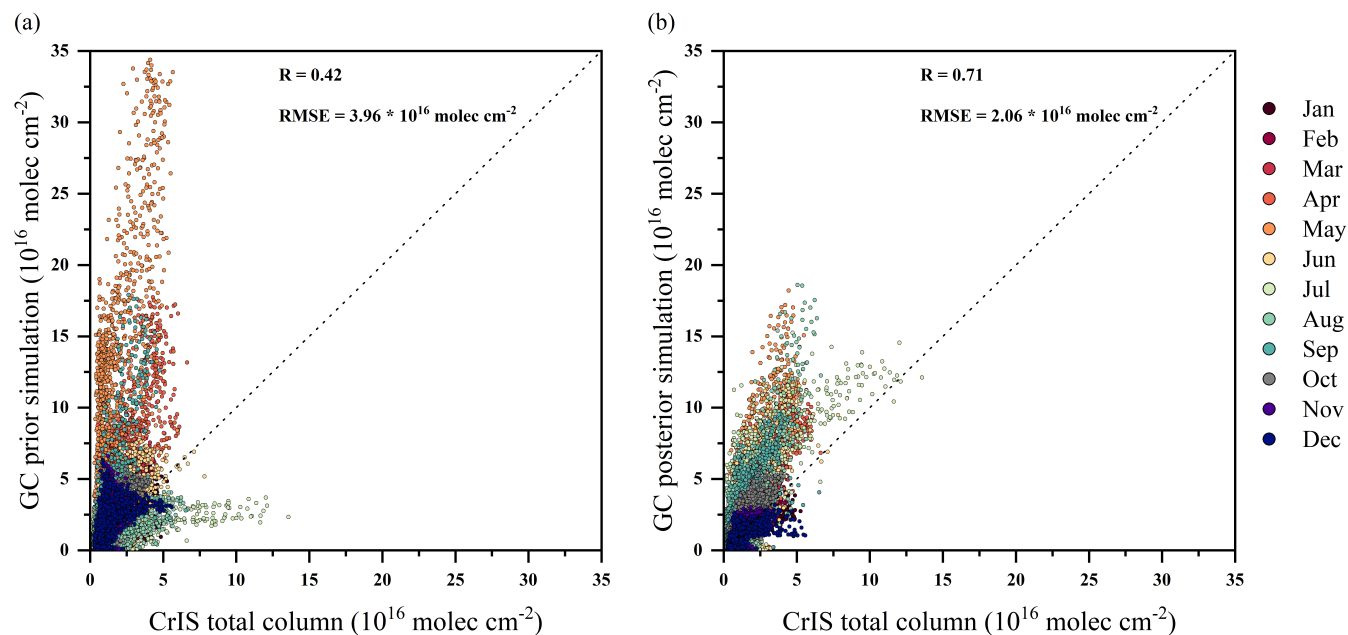


Figure 5. Scatter plot of the CrIS-observed against the NH_3 simulation over South Asia either using the prior (a) or using the posterior (b) NH_3 emission inventory from January to December.

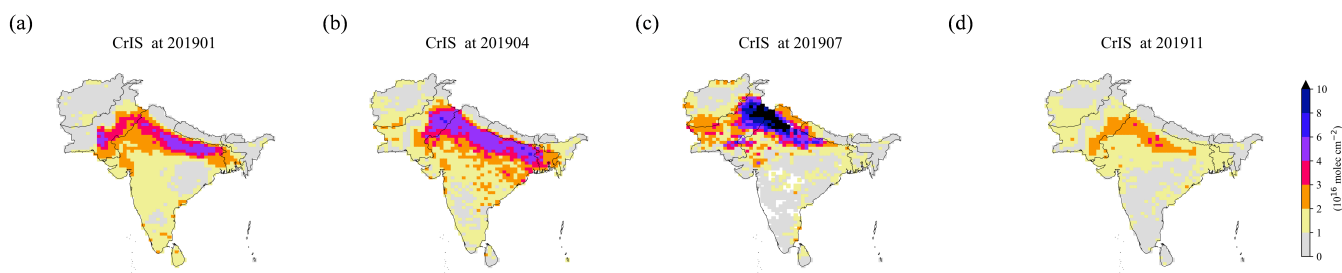


Figure 6. Spatial distribution of the CrIS-observed monthly NH_3 column in 2019 January (a), April (b), July (c) and November (d).

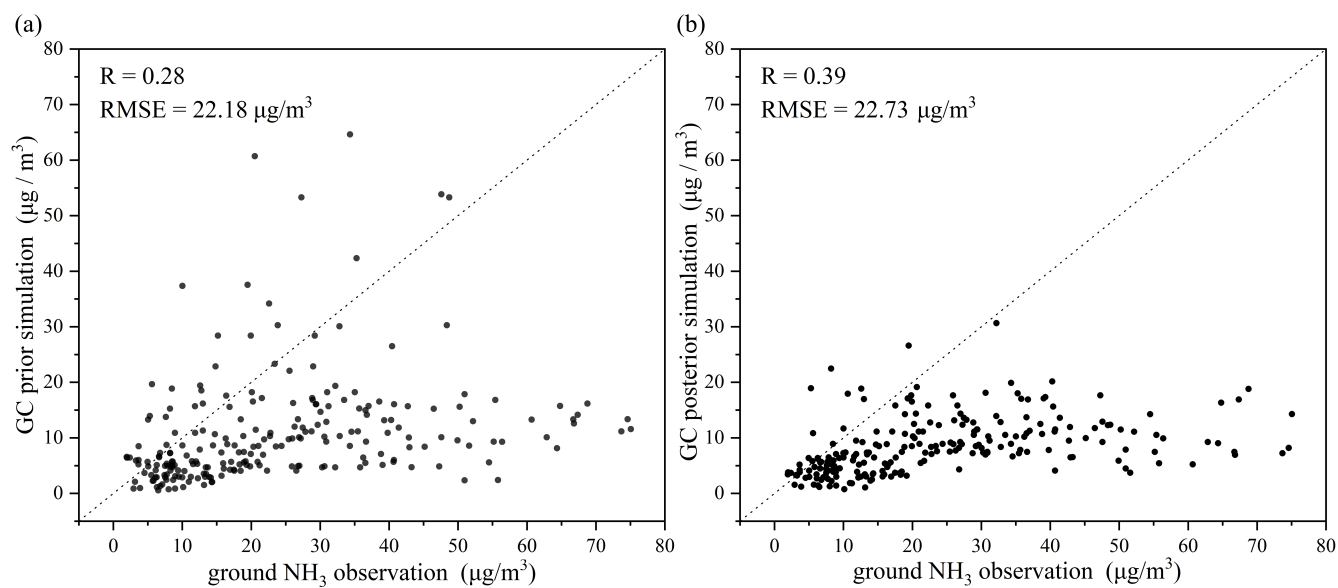


Figure 7. Scatter plot of the ground-observed against the NH_3 simulation over South Asia either using the prior (a) or using the posterior (b) NH_3 emission inventory in 2019.

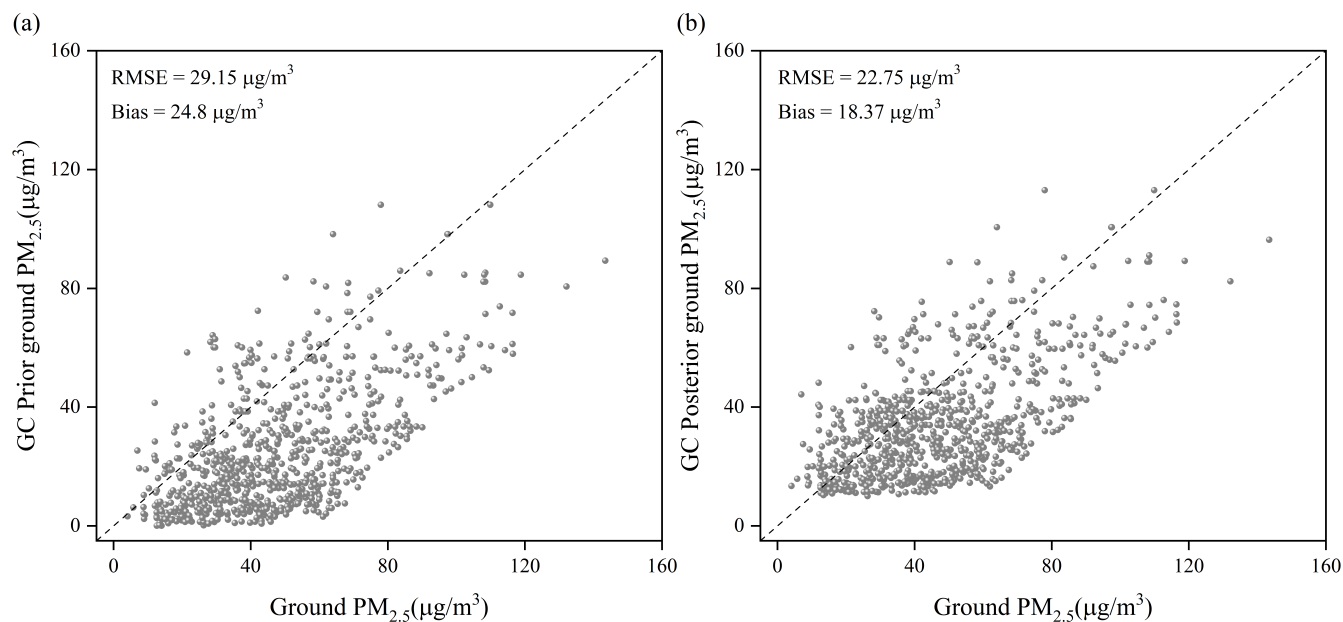


Figure 8. Scatter plot of the ground-observed against the $PM_{2.5}$ simulation over South Asia either using the prior (a) or using the posterior (b) emission inventory in 2019.

measurements. This is evident from the higher correlation coefficient ($R = 0.39$) in the posterior compared to $R = 0.28$ in the prior simulation. The RMSE values remained almost the same, changing slightly from $22.18 \mu\text{g}/\text{m}^3$ in the prior to $22.73 \mu\text{g}/\text{m}^3$ in the posterior. The large remaining error is due to several instances where ground ammonia concentration measurements indicated values several times higher than our simulations. This was also reported by Pawar et al. (2021b), which suggest

5 that ground ammonia observations are likely to overestimate ammonia levels. The mismatch between ground observations and simulations may be attributed to the fact that most monitoring stations are located in urban regions of India, where ammonia concentrations are higher due to traffic and human activities (Sharma et al., 2014). Simulations with an extremely fine resolution could provide a more accurate representation of ammonia characteristics at these surface sites. However, such simulations would significantly increase the computational burden on the emission inversion system, which is beyond the scope of this

10 study.

Ammonia is the key precursor of the inorganic aerosol. The estimated ammonia emission inventory is supposed to improve the aerosol simulation as well, under the assumption that aerosols from other sources are accurately represented. The monthly averaged $PM_{2.5}$ concentrations against the simulations either using our prior or using the posterior ammonia inventory, as shown in Fig. 8 (a-b). It is evident that both RMSE and Bias have been reduced to varying degrees: RMSE decreased from

15 $29.15 \mu\text{g}/\text{m}^3$ in the prior to $22.75 \mu\text{g}/\text{m}^3$ in the posterior, and bias decreased from $24.8 \mu\text{g}/\text{m}^3$ in the prior to $18.37 \mu\text{g}/\text{m}^3$ in the posterior. These results indicate that the emission inventory optimized by our inversion system has improved the model's performance in simulating $PM_{2.5}$, reducing both systematic biases and model underestimation effectively.



3.2 Seasonal and annual variation of ammonia concentration

We examined the monthly average of the total ammonia column concentrations simulated by the model over the South Asia region, along with IASI and CrIS observations, in Fig. 9 (a). The prior model results demonstrate significant seasonal variability in ammonia column concentrations, characterized by peaks in May and September and comparatively low levels during the summer months. This has been corrected through assimilating the IASI measurements in this study. Conversely, the posterior results reveal a distinct temporal pattern, featuring a pronounced peak in May and a negligible peak in July. The high value in May is attributed to huge amount of biomass burning in South Asia during the spring. The heavy use of fertilizers in agricultural activities, combined with higher temperatures, has resulted in the highest emission throughout the year, as will be illustrated in Fig. 9 (b) in Section 3.3. This has lead to the second ammonia concentration peak in July. The reasons for higher emissions in July but lower concentration levels compared to May could be attributed to meteorological factors. The monsoon season in South Asia results in increased wet deposition, and notably, 2019 experienced the most intense monsoon since 1994 (NASA, 2020). Additionally, CrIS also exhibits minor peaks in May and July, consistent with our posterior results.

Fig. 10 (a-i) illustrates the annual average NH_3 column concentrations observed by the IASI satellite instruments from 2015 to 2023. The data clearly show that Pakistan and northern India consistently experience the highest ammonia concentrations, with values exceeding 5×10^{16} molec cm^{-2} . Furthermore, the spatial distribution of annual average ammonia column concentrations has remained relatively stable over the past decade.

Fig. 10 (j) depicts the monthly mean ammonia column concentrations derived from the IASI satellite. The time series reveals a clear seasonal pattern, with peaks occurring in summer and lower levels in winter, and the highest concentrations consistently observed in July. Additionally, the inter-annual variation in ammonia column concentrations from 2013 to 2019 exhibits a modest upward trend, ranging from 2.17 to 2.6 ($\times 10^{16}$ molec cm^{-2}), corresponding to an average growth rate of approximately 6.32%. Subsequent to 2019, ammonia concentrations stabilize within the range of 2.6 to 2.8 ($\times 10^{16}$ molec cm^{-2}). Given the relatively stable ammonia levels after 2019, we restricted our analysis to conducting an assimilation-based emission inversion for the year 2019. Extending emission inversion over a longer period would require substantial computational resources.

3.3 Spatial and Seasonal variation of ammonia emission

By assimilating IASI ammonia column concentrations, the posterior monthly ammonia emission inventories for 2019 were updated. Scenarios of the posterior emission inventories, along with the increments (posterior minus prior), for January, April, July, and November are shown in Fig. 3 (b)-(c). The prior, posterior, and increment data for the remaining months of 2019 are provided in Figure S3 and S4 in the Supplementary Material. Our posterior inventory demonstrated that the primary sources of ammonia originated from North India, Pakistan, and Bengal in general. This finding is consistent with the CEDS inventory, as well as with other studies (Pawar et al., 2021a). However, huge discrepancy are presented when we compared the posterior and prior result, particular in April in Fig. 3(b) and July in Fig. 2(c). The posterior results reveal a distinct seasonal

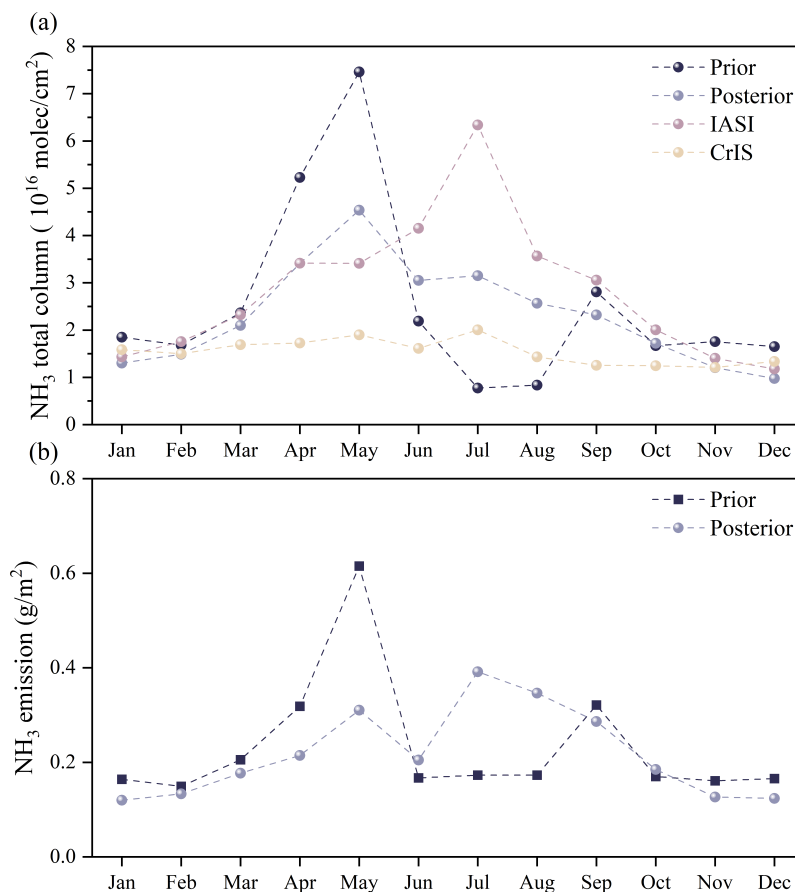


Figure 9. The monthly average total ammonia column concentrations from the prior and posterior, IASI-observed, and CrIS-observed from January to December (a). The monthly average values of prior and posterior emissions from January to December (b).

emission profile compared to the prior. Specifically, emissions during the spring are significantly overestimated in the prior model, whereas summer emissions are underestimated by up to threefold.

To better illustrate the differences in timing profiles throughout the year, the monthly average emission intensity over South Asia was calculated and is shown in Fig. 9 (b). The prior emission inventory exhibits a "double-peak" pattern, mirroring the profile of the average ammonia concentration displayed in Fig. 9 (a). The emission flux reaches its maximum in May, peaking at approximately 0.6 g/m², with a secondary peak occurring in September around 0.25 g/m². In contrast, the assimilation that integrates prior CEDS emissions with IASI measurements shows much lower intensities from January to May, with the largest negative differences (> 0.3 g/m²) observed in May. While the prior emissions remain relatively low during the summer, the emission inversion reveals positive increments, with the posterior inventory indicating the maximum emission flux in July, peaking at approximately 0.4 g/m². In general, the posterior emissions also display a "double-peak" pattern; however, the peaks occur in May and July, in contrast to the May and September peaks observed in the prior emissions.

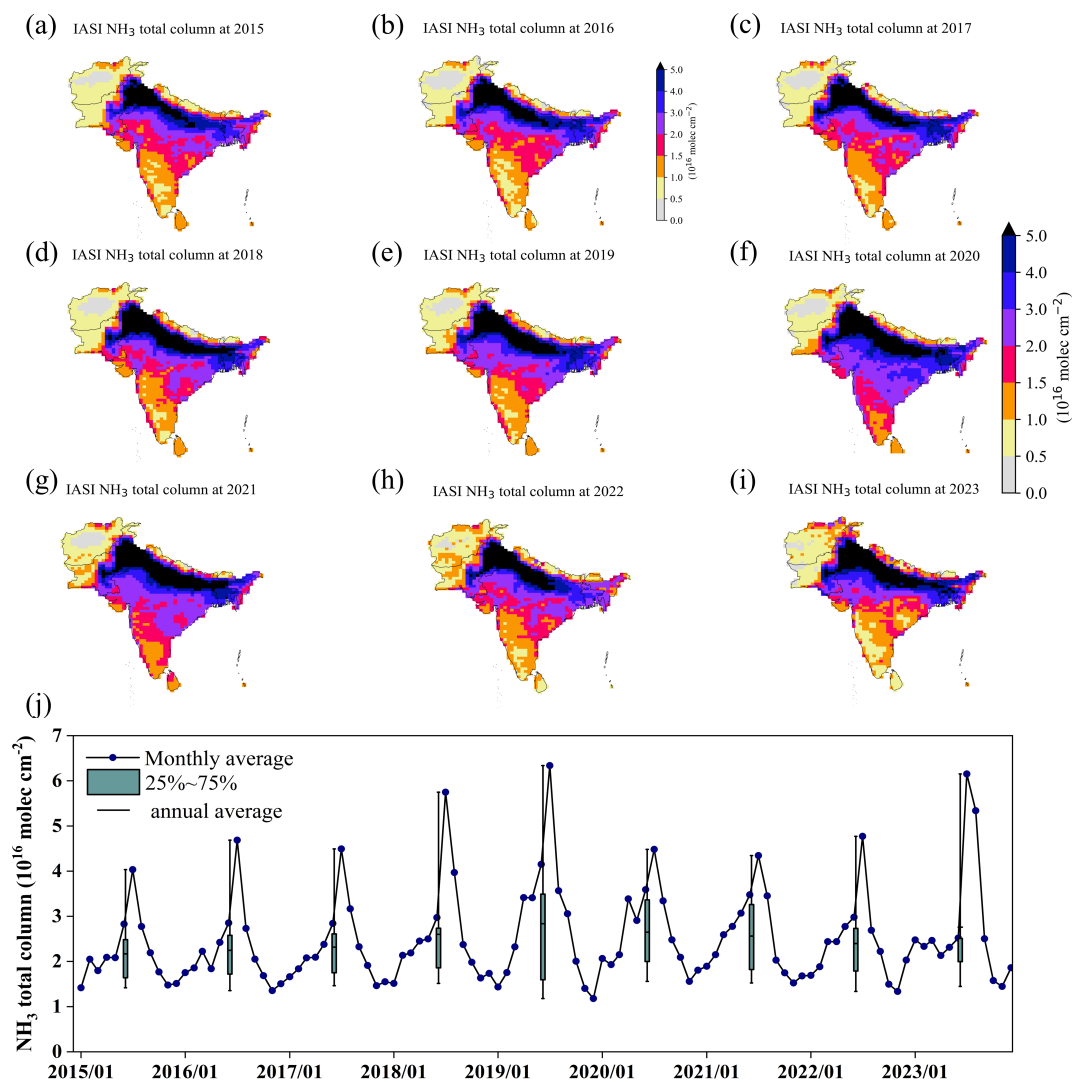


Figure 10. Spatial distribution of the annual averaged IASI column concentrations in South Asia ranging from 2015 to 2023, (a) to (i). The scatter plot (j) depicts the monthly variation in IASI-observed ammonia column concentrations from 2015 to 2023, with the box plot representing interannual changes.



The substantial emissions in July, as indicated by the posterior inventory, can be attributed to the increased fertilizer application for rice crops during the summer season (Tanvir et al., 2019). While biomass burning emissions are generally higher in spring, agricultural activities remain the primary contributors to ammonia emissions (Huang et al., 2016), resulting in July surpassing May in emission intensity. From July to September, as rice and other crops progress through their growth stages, fertilizer application typically decreases, leading to a gradual reduction in ammonia emissions. Additionally, temperatures decline from August to September, reducing the volatilization rate of ammonia. This pattern occurs because ammonia volatilization is strongly influenced by temperature (Fan et al., 2011).

The convergence of prior and posterior emission intensities in June is attributed to the overall offsetting of negative and positive increments in the region, as shown in Figure S4 (f). As depicted in panel (c) of Fig. 3, the negative increments observed in January and April primarily originate from the Indian region, while the positive increments in July and September are predominantly observed in the same area.

4 Summary and conclusion

South Asia has been severely affected by ammonia, which has significant impacts on both human health and the ecological environment. The current emission inventories, primarily based on bottom-up approaches, are subject to substantial uncertainties. This is due to the fact that the intensity of NH_3 emissions from livestock and fertilizers is heavily influenced by management and farming practices, yet this information is often not widely available. As a result, accurately simulating the spatiotemporal characteristics of atmospheric ammonia and evaluating its impacts remains challenging. The use of satellite observations, such as those from IASI, for top-down emission inversion has emerged as an effective method to develop more accurate inventories. However, research in this area remains limited in South Asia.

This study employed a 4D-EnVar-based emission inversion system to optimize ammonia emissions in South Asia. The most likely posterior monthly ammonia emission inventories were calculated given the the CEDS prior inventory and the ammonia column concentration observations from the polar-orbiting IASI satellite instrument. Validation against satellite and ground-based observations shows that ammonia concentration simulations driven by the posterior emissions perform significantly better than those driven by the prior inventory. In the comparison against the IASI measurements, the correlation coefficient (r) increased from 0.33 (for the prior) to 0.76, and the root mean square error (RMSE) was reduced from 4.64×10^{16} molec cm^{-2} (prior) to 2.48×10^{16} molec cm^{-2} (posterior). The posterior results also show improvements when compared to independent CrIS satellite measurements, with the correlation coefficient (r) rising from 0.42 (prior) to 0.71, and RMSE reducing from 3.96×10^{16} molec cm^{-2} (prior) to 2.06×10^{16} molec cm^{-2} (posterior). Additionally, validation with ground-level ammonia and $\text{PM}_{2.5}$ concentrations further supports the findings, demonstrating that our emission inversion system effectively reduces systematic biases and underestimation in ground-level simulations.

The spatial and temporal characteristics of ammonia emissions over South Asia were then analyzed based on the inversion. While the prior CEDS inventory generally captured the ammonia emission hotspots, such as in Pakistan, North India, and Bengal, it failed to accurately represent the seasonal trend. Specifically, the prior inventory showed a "double-peak" pattern



throughout the year, with peaks in May and September. In contrast, the posterior results revealed the correct seasonal pattern with the "double-peak" profile occurring in May and July.

The top-down ammonia emission inversion system driven by IASI observations has demonstrated superior performance in enhancing the ammonia emission estimates. Nevertheless, several challenges persist, such as the requirement for simulations at
5 finer resolutions to precisely capture very local emission dynamics. Furthermore, observations from stationary satellites, such as FY-4B, also deserve attention for exploring the diurnal variations of the ammonia emission.

Code and data availability

The ammonia emission inversion system is in the Python environment and is archived on Zenodo (<https://doi.org/10.5281/zenodo.7015397>). The IASI ANNI-NH₃-v4R-ERA5 data suites are available at <https://iasi.aeris-data.fr/>. The CrIS v1.6.4 data
10 are available at https://hpfx.collab.science.gc.ca/~mas001/satellite_ext/cris/. The observed NH₃ and PM_{2.5} concentrations data is available at <https://www.kaggle.com/datasets/abhisheksjha/time-series-air-quality-data-of-india-2010-2023?select=AP001.csv>.

Acknowledgments

This work is supported by the National Natural Science Foundation of China (Grant No.42475150) and Natural Science
15 Foundation of Jiangsu Province (Grant No. BK20220031).

Competing interests

The authors declare that they have no conflict of interest.



References

- Amos, H. M., Jacob, D. J., Holmes, C., Fisher, J. A., Wang, Q., Yantosca, R. M., Corbitt, E. S., Galarneau, E., Rutter, A., Gustin, M., et al.: Gas-particle partitioning of atmospheric Hg (II) and its effect on global mercury deposition, *Atmospheric Chemistry and Physics*, 12, 591–603, 2012.
- 5 Asman, W. A., Sutton, M. A., and Schjorring, J. K.: Ammonia: emission, atmospheric transport and deposition, *The New Phytologist*, 139, 27–48, 1998.
- Bauwens, M., Stavrou, T., Müller, J.-F., De Smedt, I., Van Roozendaal, M., Van Der Werf, G. R., Wiedinmyer, C., Kaiser, J. W., Sindelarova, K., and Guenther, A.: Nine years of global hydrocarbon emissions based on source inversion of OMI formaldehyde observations, *Atmospheric Chemistry and Physics*, 16, 10 133–10 158, 2016.
- 10 Beale, C. A., Paulot, F., Randles, C. A., Wang, R., Guo, X., Clarisse, L., Van Damme, M., Coheur, P.-F., Clerbaux, C., Shephard, M. W., et al.: Large sub-regional differences of ammonia seasonal patterns over India reveal inventory discrepancies, *Environmental Research Letters*, 17, 104 006, 2022.
- Beer, R., Shephard, M. W., Kulawik, S. S., Clough, S. A., Eldering, A., Bowman, K. W., Sander, S. P., Fisher, B. M., Payne, V. H., Luo, M., et al.: First satellite observations of lower tropospheric ammonia and methanol, *Geophysical Research Letters*, 35, 2008.
- 15 Bey, I., Jacob, D. J., Yantosca, R. M., Logan, J. A., Field, B. D., Fiore, A. M., Li, Q., Liu, H. Y., Mickley, L. J., and Schultz, M. G.: Global modeling of tropospheric chemistry with assimilated meteorology: Model description and evaluation, *Journal of Geophysical Research: Atmospheres*, 106, 23 073–23 095, 2001.
- Bouillon, M., Safieddine, S., Hadji-Lazaro, J., Whitburn, S., Clarisse, L., Doutriaux-Boucher, M., Coppens, D., August, T., Jacquette, E., and Clerbaux, C.: Ten-year assessment of IASI radiance and temperature, *Remote Sensing*, 12, 2393, 2020.
- 20 Bouwman, A., Lee, D., Asman, W. A., Dentener, F., Van Der Hoek, K., and Olivier, J.: A global high-resolution emission inventory for ammonia, *Global biogeochemical cycles*, 11, 561–587, 1997.
- Cao, H., Henze, D. K., Zhu, L., Shephard, M. W., Cady-Pereira, K., Damers, E., Sitwell, M., Heath, N., Lonsdale, C., Bash, J. O., et al.: 4D-Var inversion of European NH₃ emissions using CrIS NH₃ measurements and GEOS-Chem adjoint with Bi-directional and uni-directional flux schemes, *Journal of Geophysical Research: Atmospheres*, 127, e2021JD035 687, 2022.
- 25 Chaliyakunnel, S., Millet, D. B., and Chen, X.: Constraining emissions of volatile organic compounds over the Indian subcontinent using space-based formaldehyde measurements, *Journal of Geophysical Research: Atmospheres*, 124, 10 525–10 545, 2019.
- Chen, Y., Shen, H., Kaiser, J., Hu, Y., Capps, S. L., Zhao, S., Hakami, A., Shih, J.-S., Pavur, G. K., Turner, M. D., et al.: High-resolution hybrid inversion of IASI ammonia columns to constrain US ammonia emissions using the CMAQ adjoint model, *Atmospheric chemistry and physics*, 21, 2067–2082, 2021.
- 30 Choi, J., Henze, D. K., Cao, H., Nowlan, C. R., González Abad, G., Kwon, H.-A., Lee, H.-M., Oak, Y. J., Park, R. J., Bates, K. H., et al.: An inversion framework for optimizing non-methane VOC emissions using remote sensing and airborne observations in northeast Asia during the KORUS-AQ field campaign, *Journal of Geophysical Research: Atmospheres*, 127, e2021JD035 844, 2022.
- Clarisse, L., Franco, B., Van Damme, M., Di Gioacchino, T., Hadji-Lazaro, J., Whitburn, S., Noppen, L., Hurtmans, D., Clerbaux, C., and Coheur, P.: The IASI NH₃ version 4 product: averaging kernels and improved consistency, *Atmospheric Measurement Techniques*, 16, 5009–5028, <https://doi.org/10.5194/amt-16-5009-2023>, <https://amt.copernicus.org/articles/16/5009/2023/>, 2023.
- 35 Emerson, E. W., Hodshire, A. L., DeBolt, H. M., Bilsback, K. R., Pierce, J. R., McMeeking, G. R., and Farmer, D. K.: Revisiting particle dry deposition and its role in radiative effect estimates, *Proceedings of the National Academy of Sciences*, 117, 26 076–26 082, 2020.



- Eskes, H. and Boersma, K.: Averaging kernels for DOAS total-column satellite retrievals, *Atmospheric Chemistry and Physics*, 3, 1285–1291, 2003.
- Fan, X., Li, Y., and Alva, A.: Effects of temperature and soil type on ammonia volatilization from slow-release nitrogen fertilizers, *Communications in soil science and plant analysis*, 42, 1111–1122, 2011.
- 5 Fujita, R., Morimoto, S., Maksyutov, S., Kim, H.-S., Arshinov, M., Brailsford, G., Aoki, S., and Nakazawa, T.: Global and regional CH₄ emissions for 1995–2013 derived from atmospheric CH₄, $\delta^{13}\text{C-CH}_4$, and $\delta\text{D-CH}_4$ observations and a chemical transport model, *Journal of Geophysical Research: Atmospheres*, 125, e2020JD032903, 2020.
- Guttikunda, S. and Nishadh, K.: Evolution of India's PM 2.5 pollution between 1998 and 2020 using global reanalysis fields coupled with satellite observations and fuel consumption patterns, *Environmental Science: Atmospheres*, 2, 1502–1515, 2022.
- 10 Hoesly, R. M., Smith, S. J., Feng, L., Klimont, Z., Janssens-Maenhout, G., Pitkanen, T., Seibert, J. J., Vu, L., Andres, R. J., Bolt, R. M., et al.: Historical (1750–2014) anthropogenic emissions of reactive gases and aerosols from the Community Emissions Data System (CEDS), *Geoscientific Model Development*, 11, 369–408, 2018.
- Huang, S., Lv, W., Bloszies, S., Shi, Q., Pan, X., and Zeng, Y.: Effects of fertilizer management practices on yield-scaled ammonia emissions from croplands in China: a meta-analysis, *Field crops research*, 192, 118–125, 2016.
- 15 Jimenez, J. L., Canagaratna, M., Donahue, N., Prevot, A., Zhang, Q., Kroll, J. H., DeCarlo, P. F., Allan, J. D., Coe, H., Ng, N., et al.: Evolution of organic aerosols in the atmosphere, *science*, 326, 1525–1529, 2009.
- Jin, J., Fang, L., Li, B., Liao, H., Wang, Y., Han, W., Li, K., Pang, M., Wu, X., and Lin, H. X.: 4D_{EnVar}-based inversion system for ammonia emission estimation in China through assimilating IASI ammonia retrievals, *Environmental Research Letters*, 18, 034005, 2023.
- Kharol, S. K., Dammers, E., Shephard, M. W., and Cady-Pereira, K. E.: Satellite observations of ammonia over South Asia, in: *Asian Atmospheric Pollution*, pp. 227–237, Elsevier, 2022.
- 20 Kong, L., Tang, X., Zhu, J., Wang, Z., Pan, Y., Wu, H., Wu, L., Wu, Q., He, Y., Tian, S., et al.: Improved inversion of monthly ammonia emissions in China based on the Chinese ammonia monitoring network and ensemble Kalman filter, *Environmental Science & Technology*, 53, 12529–12538, 2019.
- Krupa, S.: Effects of atmospheric ammonia (NH₃) on terrestrial vegetation: a review, *Environmental pollution*, 124, 179–221, 2003.
- 25 Li, N., Tang, K., Wang, Y., Wang, J., Feng, W., Zhang, H., Liao, H., Hu, J., Long, X., Shi, C., et al.: Is the efficacy of satellite-based inversion of SO₂ emission model dependent?, *Environmental research letters*, 16, 035018, 2021.
- Liu, H., Jacob, D. J., Bey, I., and Yantosca, R. M.: Constraints from 210Pb and 7Be on wet deposition and transport in a global three-dimensional chemical tracer model driven by assimilated meteorological fields, *Journal of Geophysical Research: Atmospheres*, 106, 12109–12128, 2001.
- 30 Liu, L., Xu, W., Lu, X., Zhong, B., Guo, Y., Lu, X., Zhao, Y., He, W., Wang, S., Zhang, X., et al.: Exploring global changes in agricultural ammonia emissions and their contribution to nitrogen deposition since 1980, *Proceedings of the National Academy of Sciences*, 119, e2121998119, 2022.
- Luo, Z., Zhang, Y., Chen, W., Van Damme, M., Coheur, P.-F., and Clarisse, L.: Estimating global ammonia (NH₃) emissions based on IASI observations from 2008 to 2018, *Atmospheric Chemistry and Physics*, 22, 10375–10388, 2022.
- 35 McDuffie, E. E., Smith, S. J., O'Rourke, P., Tibrewal, K., Venkataraman, C., Marais, E. A., Zheng, B., Crippa, M., Brauer, M., and Martin, R. V.: A global anthropogenic emission inventory of atmospheric pollutants from sector- and fuel-specific sources (1970–2017): an application of the Community Emissions Data System (CEDS), *Earth System Science Data*, 12, 3413–3442, 2020.



- Mukherjee, A. and Agrawal, M.: World air particulate matter: sources, distribution and health effects, *Environmental chemistry letters*, 15, 283–309, 2017.
- NASA: Unusual Monsoon Rains in India, <https://earthobservatory.nasa.gov/images/145703/unusual-monsoon->, accessed: 2024-12-02, 2020.
- Park, R. J., Jacob, D. J., Field, B. D., Yantosca, R. M., and Chin, M.: Natural and transboundary pollution influences on sulfate-nitrate-ammonium aerosols in the United States: Implications for policy, *Journal of Geophysical Research: Atmospheres*, 109, 2004.
- 5 Pawar, P. V., Ghude, S. D., Jena, C., Möring, A., Sutton, M. A., Kulkarni, S., Lal, D. M., Surendran, D., Van Damme, M., Clarisse, L., Coheur, P.-F., Liu, X., Govardhan, G., Xu, W., Jiang, J., and Adhya, T. K.: Analysis of atmospheric ammonia over South and East Asia based on the MOZART-4 model and its comparison with satellite and surface observations, *Atmospheric Chemistry and Physics*, 21, 6389–6409, <https://doi.org/10.5194/acp-21-6389-2021>, <https://acp.copernicus.org/articles/21/6389/2021/>, 2021a.
- 10 Pawar, P. V., Ghude, S. D., Jena, C., Möring, A., Sutton, M. A., Kulkarni, S., Lal, D. M., Surendran, D., Van Damme, M., Clarisse, L., Coheur, P.-F., Liu, X., Govardhan, G., Xu, W., Jiang, J., and Adhya, T. K.: Analysis of atmospheric ammonia over South and East Asia based on the MOZART-4 model and its comparison with satellite and surface observations, *Atmospheric Chemistry and Physics*, 21, 6389–6409, <https://doi.org/10.5194/acp-21-6389-2021>, <https://acp.copernicus.org/articles/21/6389/2021/>, 2021b.
- Qu, Z., Henze, D. K., Theys, N., Wang, J., and Wang, W.: Hybrid mass balance/4D-Var joint inversion of NO_x and SO₂ emissions in East Asia, *Journal of Geophysical Research: Atmospheres*, 124, 8203–8224, 2019.
- 15 Rodgers, C. D.: *Inverse methods for atmospheric sounding: theory and practice*, vol. 2, World scientific, 2000.
- Sanderson, M. G., Collins, W. J., Johnson, C. E., and Derwent, R. G.: Present and future acid deposition to ecosystems: The effect of climate change, *Atmospheric Environment*, 40, 1275–1283, 2006.
- Sharma, S. K., Kumar, M., Rohtash, Gupta, N., Saraswati, Saxena, M., and Mandal, T.: Characteristics of ambient ammonia over Delhi, India, *Meteorology and Atmospheric Physics*, 124, 67–82, 2014.
- 20 Spandana, B., Rao, S. S., Upadhyaya, A. R., Kulkarni, P., and Sreekanth, V.: PM_{2.5}/PM₁₀ ratio characteristics over urban sites of India, *Advances in Space Research*, 67, 3134–3146, 2021.
- Tanvir, A., Khokhar, M. F., Javed, Z., Sandhu, O., Mustansar, T., and Shoaib, A.: Spatiotemporal evolution of atmospheric ammonia columns over the Indo-Gangetic plain by exploiting satellite observations, *Advances in Meteorology*, 2019, 2019.
- 25 Van Damme, M., Clarisse, L., Heald, C. L., Hurtmans, D., Ngadi, Y., Clerbaux, C., Dolman, A. J., Erisman, J. W., and Coheur, P. F.: Global distributions, time series and error characterization of atmospheric ammonia (NH₃) from IASI satellite observations, *Atmospheric Chemistry and Physics*, 14, 2905–2922, <https://doi.org/10.5194/acp-14-2905-2014>, <https://acp.copernicus.org/articles/14/2905/2014/>, 2014.
- Van Damme, M., Whitburn, S., Clarisse, L., Clerbaux, C., Hurtmans, D., and Coheur, P.-F.: Version 2 of the IASI NH₃ neural network retrieval algorithm: near-real-time and reanalysed datasets, *Atmospheric Measurement Techniques*, 10, 4905–4914, <https://doi.org/10.5194/amt-10-4905-2017>, <https://amt.copernicus.org/articles/10/4905/2017/>, 2017.
- 30 von Clarmann, T. and Glatthor, N.: The application of mean averaging kernels to mean trace gas distributions, *Atmospheric Measurement Techniques*, 12, 5155–5160, 2019.
- Wang, Y. and Jacob, D. J.: Anthropogenic forcing on tropospheric ozone and OH since preindustrial times, *Journal of Geophysical Research: Atmospheres*, 103, 31 123–31 135, 1998.
- 35 Wecht, K. J., Jacob, D. J., Frankenberg, C., Jiang, Z., and Blake, D. R.: Mapping of North American methane emissions with high spatial resolution by inversion of SCIAMACHY satellite data, *Journal of Geophysical Research: Atmospheres*, 119, 7741–7756, 2014.
- Wesely, M. and Lesht, B.: Comparison of RADM dry deposition algorithms with a site-specific method for inferring dry deposition, *Water, Air, and Soil Pollution*, 44, 273–293, 1989.



- Whitburn, S., Van Damme, M., Clarisse, L., Bauduin, S., Heald, C., Hadji-Lazaro, J., Hurtmans, D., Zondlo, M. A., Clerbaux, C., and Coheur, P.-F.: A flexible and robust neural network IASI-NH₃ retrieval algorithm, *Journal of Geophysical Research: Atmospheres*, 121, 6581–6599, 2016.
- Xu, R., Tian, H., Pan, S., Prior, S. A., Feng, Y., Batchelor, W. D., Chen, J., and Yang, J.: Global ammonia emissions from synthetic nitrogen fertilizer applications in agricultural systems: Empirical and process-based estimates and uncertainty, *Global change biology*, 25, 314–326, 2019.
- Xue, T., Geng, G., Han, Y., Wang, H., Li, J., Li, H.-t., Zhou, Y., and Zhu, T.: Open fire exposure increases the risk of pregnancy loss in South Asia, *Nature communications*, 12, 3205, 2021.
- Yamaji, K., Ohara, T., and Akimoto, H.: Regional-specific emission inventory for NH₃, N₂O, and CH₄ via animal farming in South, Southeast, and East Asia, *Atmospheric Environment*, 38, 7111–7121, 2004.
- Yan, X., Akimoto, H., and Ohara, T.: Estimation of nitrous oxide, nitric oxide and ammonia emissions from croplands in East, Southeast and South Asia, *Global Change Biology*, 9, 1080–1096, 2003.
- Zhang, X., Wu, Y., Liu, X., Reis, S., Jin, J., Dragosits, U., Van Damme, M., Clarisse, L., Whitburn, S., Coheur, P.-F., et al.: Ammonia emissions may be substantially underestimated in China, *Environmental Science & Technology*, 51, 12 089–12 096, 2017.